FRONTIERS OF PHYSICS

RESEARCH ARTICLE
Volume 17 / Issue 5 / 53510 / 2022

# High efficiency giant magnetoresistive device based on two-dimensional MXene ($Mn_2NO_2$)

Xiaolin Zhang[1], Pengwei Gong[1], Fangqi Liu[1], Kailun Yao[2], Jian Wu[3], Sicong Zhu[1,†]

1 The State Key Laboratory for Refractories and Metallurgy, Hubei Province Key Laboratory of Systems Science in Metallurgical Process, Collaborative Innovation Center for Advanced Steels, International Research Institute for Steel Technology, Wuhan University of Science and Technology, Wuhan 430081, China
2 Wuhan National High Magnetic Field Center and School of Physics, Huazhong University of Science and Technology, Wuhan 430074, China
3 College of Advanced Interdisciplinary Studies, National University of Defense Technology, Changsha 410073, China
Corresponding author. E-mail: †sczhu@wust.edu.cn
Received February 23, 2022; accepted June 3, 2022

© Higher Education Press 2022

**ABSTRACT**

Due to the unique electronic structure of half-metals, characterized by the conductivity of majority-spin and the band gap of minority-spin, these materials have emerged as suitable alternatives for the design of efficient giant magnetoresistive (GMR) devices. Based on the first-principles calculations, an excellent GMR device has been designed by using two-dimensional (2D) half-metal $Mn_2NO_2$. The results show that $Mn_2NO_2$ has sandwiched between the Au/$n$$Mn_2NO_2$ ($n$ = 1, 2, 3)/Au heterojunction and maintains its half-metallic properties. Due to the half-metallic characteristics of $Mn_2NO_2$, the total current of the monolayer device can reach up to 1500 nA in the ferromagnetic state. At low voltage, the maximum GMR is observed to be $1.15 \times 10^{31}$ %. Further, by increasing the number of layers, the ultra-high GMR at low voltage is still maintained. The developed device is a spintronic device exhibiting the highest magnetoresistive ratio reported theoretically so far. Simultaneously, a significant negative differential resistance (NDR) effect is also observed in the heterojunction. Owing to its excellent half-metallic properties and 2D structure, $Mn_2NO_2$ is an ideal energy-saving GMR material.



**Keywords** half-metals, $Mn_2NO_2$, giant magnetoresistive

## 1 Introduction

The devices with high magnetic resistance (MR) play a key role in data storage and magnetic induction electronic equipment [1–4]. In such devices, the resistive random access memory is represented by the magnetic tunnel junction (MTJ) [5], in which the relatively parallel and antiparallel spin structures can produce two different resistance states to carry information, and the larger MR can provide higher sensitivity for practical applications [6–8]. Concerning high spin-polarized materials [9], the half-metals are the most prospective candidate materials, as their energy band structure is metallic in one spin channel and semiconductor or insulating in the other

*Special Topic: MXene and Its Applications (Eds.: Qing Huang, Ju Han Lee & Guangcun Shan).

Higher Education Press

https://doi.org/10.1007/s11467-022-1184-z

spin channel, thereby resulting in 100% spin polarization of electrons at the Fermi level [10]. Therefore, for half-metals, in case the magnetization directions of the two layers are the same, the electrons in the majority-spin subbands in one magnetic layer will enter the empty state of the majority-spin subbands in the other magnetic layer. Thus, the total tunneling current will be particularly large [Fig. 1(a)]. If the magnetization of the two magnetic layers is in opposite directions, another behavior is observed. Neither the majority of electrons in the spin band of one magnetic layer nor the minority of electrons in the spin band will enter the vacant state in the other magnetic layer. Thus, the tunneling current in this state will be extremely small [Fig. 1(b)]. The half-metallic materials can lead to a great difference in the current of two different magnetization states. Therefore, the devices with half-metals are observed to produce the MR effect [10–12]. In the current recent advances in magnetic tunnel junctions of two-dimensional materials for spintronics, the MR value can reach 4000 % in the device of Yan *et al.* [13] with Cu as the electrode, $CrI_3$ as the free layer and pinning layer, and h-BN as the blocking layer. The magnetoresistance can reach $10^{13}$ % in the Dirac spin gapless semiconductor $VCl_3$-based devices studied by Feng *et al.* [14]. The recently reported $Li_{0.5}CrI_3$ and $CrI_3$ devices can obtain an MR value of $10^{14}$ %, which is the highest reported MR value so far [15]. Although their research has reached an ideal MR value, the larger MR means that it can provide higher sensitivity to the device, which is also the importance of our research. The devices constructed from half-metals may also produce an obvious negative differential resistance effect (NDR), associated with electron transfer. In a specific bias range, the current of the device decreases by increasing the voltage [16–20]. The NDR effect has important applications in amplifiers, logic gates, switching devices, and other fields.

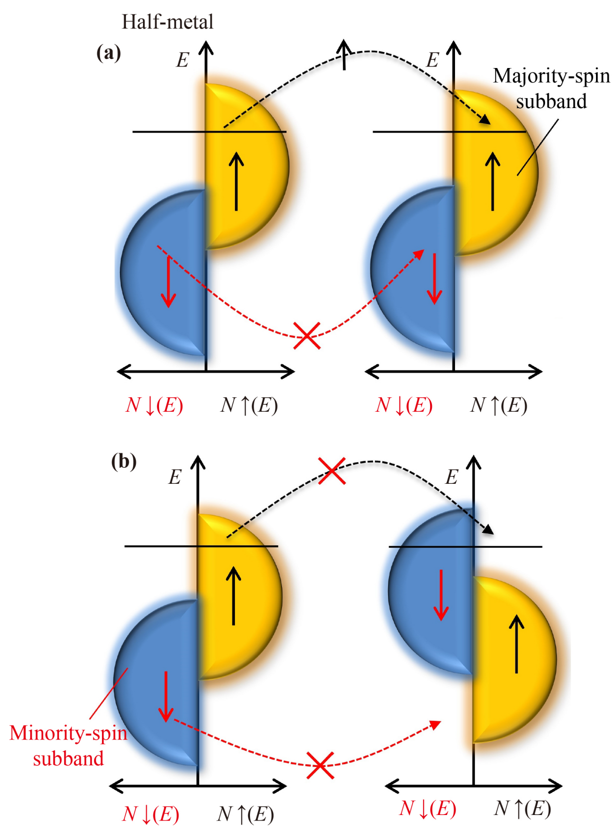


**Fig. 1** The principle of MR effect, **(a)** ferromagnetic state electron transport of half-metal. **(b)** Anti-ferromagnetic state electron transport of half-metal.

MXenes, the recently discovered two-dimensional (2D) layered transition metal C or N compounds, possess abundant magnetic and electronic properties [19–23]. MXene single-molecule films are formed by decomposing three-dimensional $M_{n+1}AX_n$ ($n$=1, 2, 3) or MAX crystal layers [24]. In MAX crystals, "M" stands for transition metals, "A" represents the group A elements, and "X" represents the C or N atoms. The 2D MXene surface is engendered by removing the group A elements of the MAX crystal by employing various methods. Depending on the etchant, the F, O, or OH groups can be terminated [25]. The high strength and flexibility of MXene make it an excellent candidate for electronics and spintronics. The MXenes studied by Qin *et al.* [26] have proven to be excellent sensing materials in the field of sensors, and they have developed an ultra-high sensitivity flexible pressure sensor based on MXene material [27]. It has promising applications in ultra-high sensitivity devices and inspires the building of more sensitive MR devices using MXene [28]. Moreover, $Ni_2NT_2$ [29], $Mn_2NT_2$ (T= O, OH, F) [30], $Ti_2NO_2$ [31], and $Cr_2NO_2$ [26] have also been reported to be functional half-metallic materials.

$Mn_2NT_2$ materials are ideal for spintronic applications, as their magnetism does not depend on the surface terminals. Among these, $Mn_2NO_2$ is a material with half-metal transport properties, which has inherent half-metal properties and does not require any external conditions, such as a strong electric field [32] or doping [33]. To develop practical spintronic devices, a few basic issues need to be considered. The Curie temperature of the half-metallic materials should be sufficiently high, i.e., enough, significantly higher than room temperature. In the theoretical calculations, the Curie temperature of $Mn_2NO_2$ reaches 1379 K [34], thus, suggesting it to be a potential magnetoresistive material [35]. In particular, the majority-spin state of $Mn_2NO_2$ is highly occupied at the Fermi level, while the minority-spin state demonstrates a very large band gap. Therefore, the electronic structure of $Mn_2NO_2$ fully meets the requirements of the high MR devices. The $Mn_2NO_2$ material is perfectly suited as a regulating magnetoresistance, but no magnetoresistance studies related to $Mn_2NO_2$ have been reported so far, so we must study its transport mechanism. In this respect, a systematic theoretical analysis is needed to evaluate the effectiveness and potential performance of $Mn_2NO_2$.

In this study, the $Mn_2NO_2$ structure is considered a potential MR material. First, we analyze the magnetic and electronic properties of $Mn_2NO_2$ have been analyzed. As Au is one of the most commonly used electrodes in the MR devices [36] and has a small lattice mismatch [37], $Mn_2NO_2$ can provide a stable geometrical structure with Au electrodes. In addition, $Mn_2NO_2$ can still maintain the half-metallic properties in the Au/$n$$Mn_2NO_2$ ($n$=1, 2, 3)/Au structure, which is suitable for MR devices. The non-equilibrium Green's function method has been employed to calculate the electron transport and magnetoresistance characteristics in the ferromagnetic and antiferromagnetic states. Finally, the MR value of the device is calculated to be very large for a small bias voltage, along with a notable NDR effect.

## 2 Calculation method

Use density functional theory (DFT) for structural optimization, which is implemented in Atom Toolkit (ATK) [38]. Use generalized gradient approximation (GGA-PBE) functional and projected enhanced wave (PAW) potential. Perform ion relaxation until the force starts, and perform ion relaxation until the applied force is less than 0.02 eV/Å per atom. Dudarev's GGA+$U$ method is used to introduce strong electron-electron interactions into transition metal atoms. The $U$ value we calculate is derived from former studies in the literature, with Mn of 3 eV [34]. To optimize the volume structure, a set of 10× 10×5 k points is used to sample the Brillouin zone. We also use VASP to calculate the electronic properties of $Mn_2NO_2$ in the previous model (Fig. S1). Then, the spin-resolved electron transport properties of these junctions are studied in the form of Krdsch non-equilibrium Green's function (NEGF) implemented in the ATK. The width of the tunneling region increases with the number $n$ of $Mn_2NO_2$ units in the junction [39], where $n$=1, 2, or 3.

Apply the Landauer–Buttiker equation from the NEGF method to calculate the current produced by the applied voltage $I$ ($V_b$). The $T$ ($E$, $V_b$) is the probability of electron transport when energy $E$ is applied at bias voltage $V_b$. The $f_{L(R)}$ is the Fermi–Dirac distribution function and $\mu_{L(R)}$ is the chemical potential of the left (right) electrode:

$$I(V_b)=\frac{2e^2}{h}\int_{-\infty}^{\infty}T\left(E,V_b\right)\left[f_L\left(E-\mu_L\right)-f_R(E-\mu_R)\right]\mathrm{d}E. \tag{1}$$

## 3 Results and discussion

### 3.1 Structural and electronic properties

First, we analyze the basic characteristics of $Mn_2NO_2$, such as structure and density of states (DOS) (Fig. 2). The properties indicate that $Mn_2NO_2$ is metallic in the majority spin, and there is a very large band gap of 3.2 eV in the minority spin. There is 100% spin polarization around the Fermi level, which meets the design requirements of MR devices. The first step in designing an MR device based on $Mn_2NO_2$ is to analyze the electrical characteristics of the Au electrode in contact with $Mn_2NO_2$. In our calculation, the Au–$Mn_2NO_2$–Au device is Au (111) in contact with $Mn_2NO_2$, and the lattice mismatch rate is less than 4%. To find the most stable binding mode at the interface, the interaction between three different sites (the top sites of O, N, and Mn) with high symmetry on $Mn_2NO_2$ and the Au atoms is considered. After structural optimization, the position at the top of O is the most advantageous. At the same time, we optimize the distance of Au–O and find that the bond length tends to be 2.3 Å, so we adjust the distance between the Au electrode and $Mn_2NO_2$ to 2.3 Å and then optimize it. Finally, the Au–O bond length in the device is between 2.3–2.33 Å (Table S1). The calculated lattice parameters of $Mn_2NO_2$ and Au are 2.98 Å and 2.88 Å, respectively. A lattice mismatch of 3.2% is ideal as it has almost no effect on the electronic structure of the entire device. When building the bilayer device, we study three stacking configurations of the bilayer of $Mn_2NO_2$ (Fig. S3). The adhesion energy ($E_{AD}$) is used to characterize the interaction between different layers and can be calculated by the following equation:

$$E_{AD}=\frac{E\left(\text{layer 1}\right)+E\left(\text{layer 2}\right)-E\left(\text{total}\right)}{n}, \tag{2}$$

where $E$ (total) refers to the total energy of the heterojunction, $E$ (layer 1) and $E$ (layer 2) represent the total

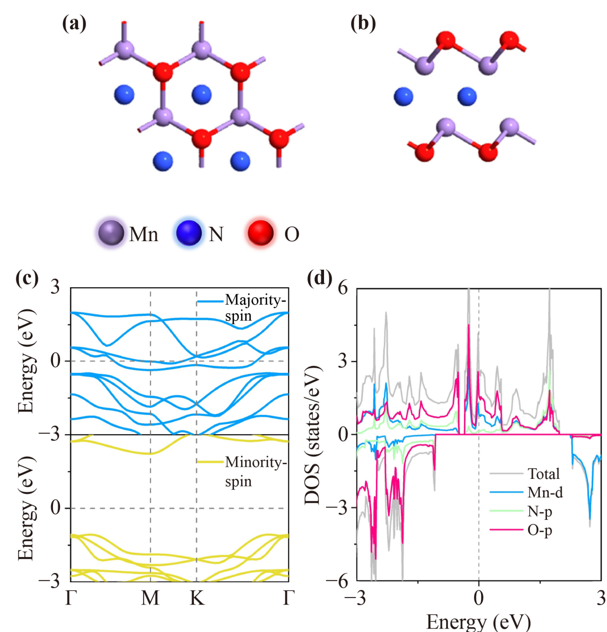


**Fig. 2** **(a)** A top and **(b)** a side views of $Mn_2NO_2$, **(c)** band structure of $Mn_2NO_2$ and **(d)** density of states of $Mn_2NO_2$.

energy of each layer in the same supercell of the corresponding structure, and $n$ represents the number of atoms in one layer. The three stacking arrangements are the top positions of Mn, N, and O atoms, respectively. For the above three configurations, the adsorption energy of Top-Mn is the largest and the layer distance is the smallest, which means that this arrangement is the most stable.

After observing the change of MR, we adjust the thickness of the device. The details of the three configurations of Au/$n$Mn$_2$NO$_2$ ($n$ = 1, 2, 3)/Au are shown in Fig. 3, which have undergone sufficient relaxation and have reached the convergence standard. The scattering area is composed of 1, 2, and 3 layers of Mn$_2$NO$_2$, and the buffer area is composed of Au (111) planes repeating for 3 layers. The two electrodes of the device are the same layer of Au (111), and the left and right electrodes respectively extend infinitely along the transport direction.

### 3.2 Electronic properties of devices

In our device, the MR is adjusted by increasing the number of Mn$_2$NO$_2$ units. Therefore, we study the influence of the electronic structure of $n$Mn$_2$NO$_2$ in Au/$n$Mn$_2$NO$_2$ ($n$=1, 2, 3)/Au heterojunction on the adhesion of Au, and evaluated their performance. As shown in Figs. 4 (a)–(c), compared with the original Mn$_2$NO$_2$, the adhesion of the Au (111) layer does have a certain effect on the DOS of the Mn$_2$NO$_2$ layer, but it does not change the half-metal properties. We calculate the projected band structure (Fig. S4) of Mn$_2$NO$_2$ after contact with Au (111), and for the system after contact, it is still mainly contributed by Mn$_2$NO$_2$ above the Fermi level, and Mn$_2$NO$_2$ contributes less below the Fermi level. This result is in good agreement with the original band structure, indicating that the attachment of the Au (111) layer to Mn$_2$NO$_2$ leads to small changes in the electronic structure near the Fermi level and that the half-metallic properties of Mn$_2$NO$_2$ can be well preserved in the heterojunction. For Au/Mn$_2$NO$_2$/Au, the difference between the highest average potential at the contact interface and the highest average potential at the Au surface is –0.034 eV, the value is negative (Fig. S5) indicating that electrons can be easily injected from Au to Mn$_2$NO$_2$ without any potential barrier. We conclude that Au/Mn$_2$NO$_2$/Au is a good ohmic contact. In the electron localization function (ELF), the blue color in the middle of the Au/Mn$_2$NO$_2$/Au contact indicates that the chemical bond is very weak and that the interaction force at the interface is through the van der Waals force. To analyze the electron transfer at the device interface, we plot the charge difference density diagram between the middle layer of the device and the adjacent four layers of Au atoms [Fig. 4(d)]. Au atom transfers electrons to the O atom, and the Au–O bond is formed between layers. The Au/$n$Mn$_2$NO$_2$ ($n$ = 1, 2, 3)/Au interlayer has little effect on the internal electron distribution. The transferred electrons are mainly provided by Au atoms. The electrons transferred to the middle layer are mainly concentrated on O atoms, and only a small part is concentrated on Mn and N atoms.

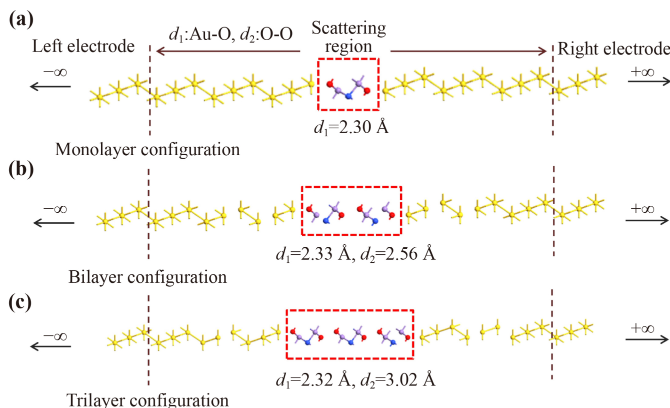


**Fig. 3** Au/$n$Mn$_2$NO$_2$ ($n$=1, 2, 3)/Au device structure diagram, after relaxation **(a)**, **(b)**, **(c)** configuration is for $n$= 1, 2, 3 configuration, respectively. The transport direction is along the $z$-axis, as shown by the left/right arrows, and the two electrodes extend to $z$=±∞.

### 3.3 Electrical transport of devices

To calculate the characterization of Au/$n$Mn$_2$NO$_2$ ($n$=1, 2, 3)/Au as a giant magnetoresistive (GMR) device, we use FM and AFM configurations to evaluate the current-voltage characteristics of the Au–MXene–Au structure. The current is calculated at a bias voltage of 0–1.0 V. As shown in Fig. 5, the current largely depends on the

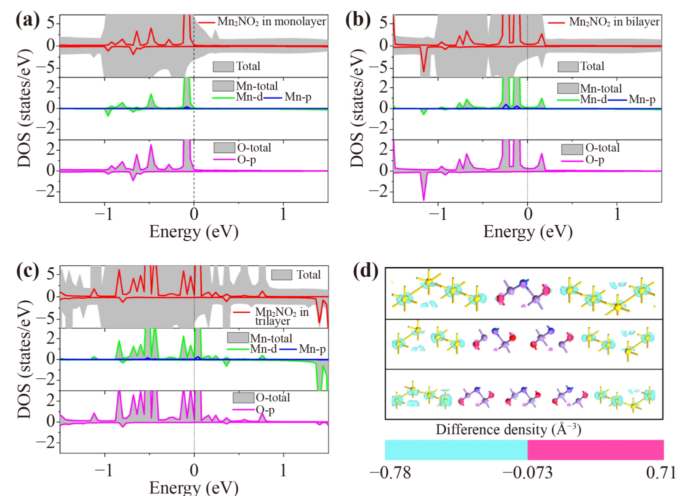


**Fig. 4** DOS of Mn$_2$NO$_2$ in **(a)** monolayer, **(b)** bilayer, and **(c)** trilayer between heterojunctions changes, and the dotted line corresponds to the Fermi level. **(d)** The charge density between the middle region of the device and the adjacent Au atoms is different. Blue indicates charge transfer and red indicates charge accumulation. The isosurface value sets to 0.03.

configuration of MXene. In FM configuration, the current of the three sandwich structures is higher than that of the corresponding AFM configuration at low bias. The spin with the same spin direction has a higher current than the spin with the opposite spin direction, which is the characteristic of MR devices. For the monolayer device [Figs. 5(a) and (b)], the FM configuration reaches the highest value when the total current is 0.4 V, while the AFM approaches zero. At 0–0.6 V, due to the huge difference between the currents of FM and AFM, this result will bring a GMR effect. In the monolayer, the device has a large current, which is attributed to the half-metallic characteristics of $Mn_2NO_2$. As previously shown, $Mn_2NO_2$ has a high spin DOS near the Fermi level. For double-layer devices [Figs. 5(c) and (d)], as the vacuum layer increases with the number of layers, the total current exhibits a two-order decrease. In fact, in the voltage range of 0.0–0.4 V, FM and AFM still maintain a large quantitative difference. At 0.1 V, the majority-spin current in AFM is much larger than the minority-spin current, and the total current value obtained is contributed by the current of the majority-spin electrons, showing a better spin filtering effect (SFE). For the three-layer device [Figs. 5(e) and (f)], the total current has dropped by four orders of magnitude. Within the bias voltage range of 0–0.2 V, the huge difference in current under different configurations continues to be maintained, and in the FM state at 0.1V bias, there is excellent SFE. Since the current of Au/$3Mn_2NO_2$/Au has dropped to a very small value, we do not further analyze the current of devices with four layers or more.

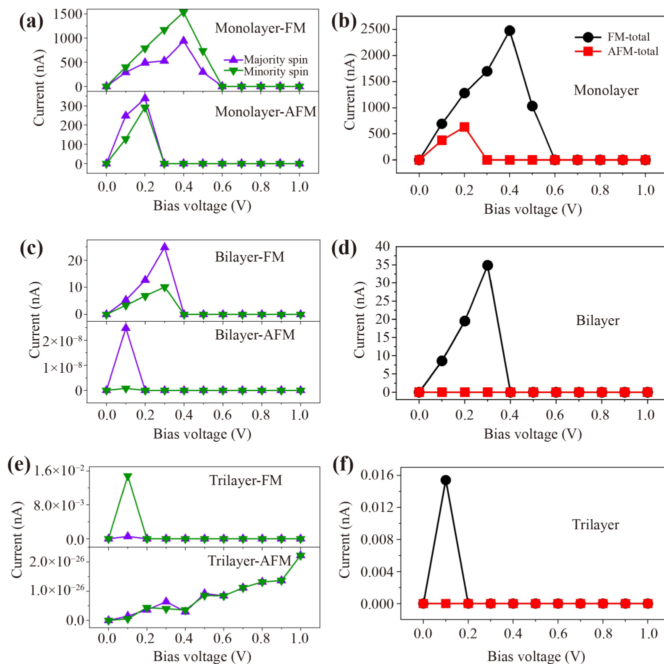


**Fig. 5** **(a, b)** are the monolayer $Mn_2NO_2$ heterojunction spin sub-current and total current, **(c, d)** are the double-layer spin sub-current and total current, and **(e, f)** are the three-layers spin sub-current and total current.

## 3.4 Giant magnetoresistance effect

The huge difference in current between ferromagnetic FM and non-ferromagnetic AFM means that Au/$n$$Mn_2NO_2$ ($n$=1, 2, 3)/Au will produce a high GMR effect. Here, GMR = $(I_{FM} - I_{AFM})$ / $I_{AFM}$ × 100%, Among them, $I_{FM}$ ($I_{AFM}$) is the total current in FM (AFM) Au/$n$$Mn_2NO_2$ ($n$=1, 2, 3)/Au. The interpolation table in Fig. 6(a) shows the GMR ratio as a function of bias voltage. This shows that in the range of applied bias voltage, the maximum GMR ratio in the monolayer device can reach $1.15\times10^{31}$ %, and the maximum GMR ratio in the bilayer and trilayer devices can reach $2.92\times10^{29}$ % and $7.46\times10^{26}$ % respectively. In devices, it is desirable to use low voltage to reduce the energy consumption of nano-devices. Obviously, with the increase in the number of layers, the devices show a very

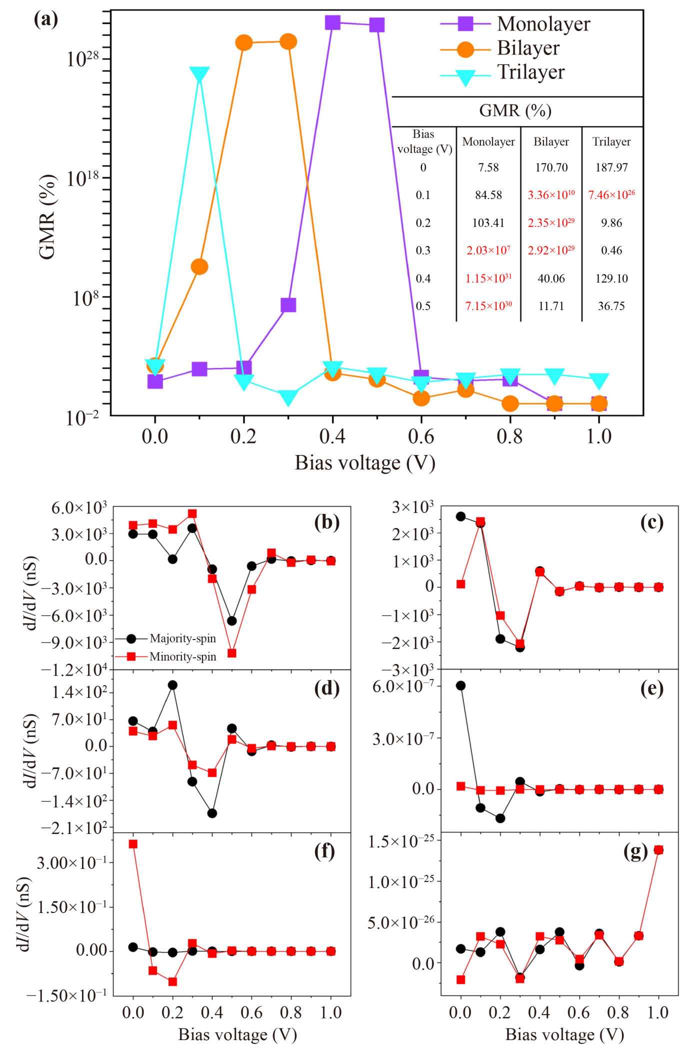


| GMR (%) | | | |
|---|---|---|---|
| Bias voltage (V) | Monolayer | Bilayer | Trilayer |
| 0 | 7.58 | 170.70 | 187.97 |
| 0.1 | 84.58 | $3.36\times10^{10}$ | $7.46\times10^{26}$ |
| 0.2 | 103.41 | $2.35\times10^{29}$ | 9.86 |
| 0.3 | $2.03\times10^{7}$ | $2.92\times10^{29}$ | 0.46 |
| 0.4 | $1.15\times10^{31}$ | 40.06 | 129.10 |
| 0.5 | $7.15\times10^{30}$ | 11.71 | 36.75 |

**Fig. 6** **(a)** The trend of GMR with the number of layers under different bias voltages and the specific values of GMR is inserted in the table. Monolayer device spin-resolved NDC **(b)** FM state and **(c)** AFM state, bilayer device spin-resolved NDC **(d)** FM state **(e)** AFM state, trilayer device spin-resolved NDC **(f)** FM state **(g)** AFM state.

**Table 1** Electron density of FM and AFM at the threshold, peak, and off voltages for monolayer, bilayer, and trilayer devices.

| Density ($Å^{-3}$) 0 1 2 | | FM | AFM |
|---|---|---|---|
| Monolayer | Threshold voltage (0 V) | | |
| | Peak voltage (0.4 V) | | |
| | Off voltage (0.6 V) | | |
| Bilayer | Threshold voltage (0 V) | | |
| | Peak voltage (0.3 V) | | |
| | Off voltage (0.4 V) | | |
| Trilayer | Threshold voltage (0 V) | | |
| | Peak voltage (0.1 V) | | |
| | Off voltage (0.2 V) | | |

high GMR effect at a lower bias voltage, showing the advantage of using $Mn_2NO_2$ at low voltage. Of course, the theoretical GMR ratio is commonly higher than the experimental value due to non-zero temperature and possible defect scattering in the experiment. And because the accuracy of the calculation software is much higher than the measurement accuracy of the actual experiment, the value when taking the GMR ratio will be very large.

As the number of layers increases, GMR has a clear pattern, that is, the peak value shifts to the left (Fig. 6). In the monolayer device, GMR reaches a high value at 0.3–0.5 V, double-layer devices have a large value at 0.1–0.3 V, while three-layer devices only have a high GMR at 0.1 V. There may be two reasons for this phenomenon: the first reason is that the thickening of the central region of the device will increase the shunting effect on the current, resulting in the rapid decline of GMR. The second reason is that too thick central regions will increase the non-spin dependent scattering of electrons, leading to the decrease of spin-dependent scattering of electrons at slightly high bias voltage, and spin-dependent scattering is the fundamental reason for GMR. Since there is an obvious negative differential resistance effect in each device (Fig. 5), we draw the curve of negative differential conductance (NDC) and voltage change in Figs. 6(b)–(g). For the monolayer device, the majority spin of the FM state decreases rapidly in the bias range of 0.4–0.6V, and the NDC values reach $-10^3$ nS and $-10^4$ nS respectively. For the AFM state, majority-spin and minority-spin currents decrease in the range of 0.2–0.3 V, and the NDC value reaches $-10^3$ nS.

For delving into the transport characteristics at the threshold, peak, and off voltages, we list the electron density of the device at these typical voltages (Table 1), intercepting four Au atoms near to show them more clearly. Similar properties are found in the monolayer, bilayer, and trilayer devices, with roving electrons in the FM and AFM states, spread throughout the transport channel at threshold voltages, showing good transport capabilities. As the voltage increases, the FM state of the device retains this property at the peak voltage, while the electronic state of the AFM all but disappears. The electronic states of both FM and AFM disappear completely at the off voltage when the device current is almost 0 nA. In addition to the electron density of the device, we also plot the DOS of the original $Mn_2NO_2$ in the FM and AFM states against the DOS of $Mn_2NO_2$ in the device (Fig. 7). It can be seen that the half-metallic

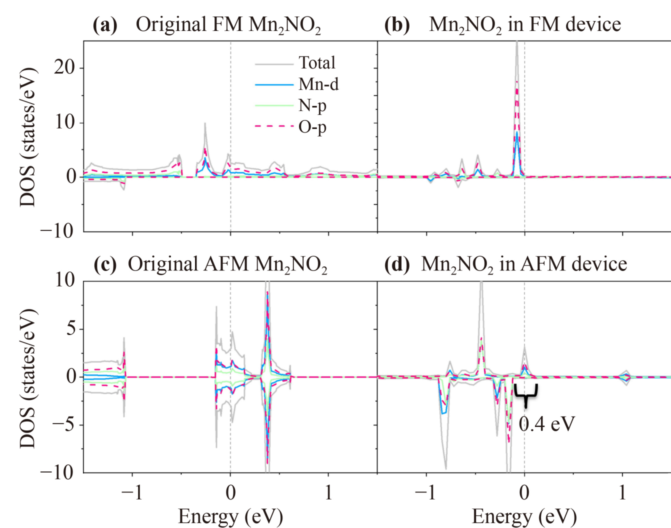


**Fig. 7** **(a)** DOS of original $Mn_2NO_2$ in the FM state, **(b)** DOS of $Mn_2NO_2$ in the FM device, **(c)** DOS of original $Mn_2NO_2$ in the AFM state, and **(d)** DOS of $Mn_2NO_2$ in the AFM device.

nature of the FM is retained in the device and the half-metallic nature of the AFM is produced, indicating that the device structure has a great influence on the magnetic properties of $Mn_2NO_2$. The AFM has a small peak at the Fermi level with a width of around [–0.1, 0.1] eV range. It is clear that the peak moves towards the Fermi level when bias is applied, so the current quickly reduces to cut-off. For the FM state, there is a very large peak in the [–0.25 eV, 0 eV] range, which remains largely in the 0–0.5 V range through the galvanic current. After the bias voltage is applied, the DOS peak moves towards the Fermi level and directly into the transmission channel, therefore, the FM state stays in the high current state for longer.

With an in-depth understanding of the changes in current and GMR values, we calculate the relevant bias transmission spectra of Au/$n$$Mn_2NO_2$ ($n$=1, 2, 3)/Au in FM or AFM arrangement (Fig. 8). Spin-dependent transmission spectra can also interpret the current-voltage characteristics. The gray dotted box in each figure represents the effective range of the transmission spectrum, which is called the bias window. Only the transmission spectrum in the bias window contributes to the current. Compared with the AFM state in Au/$n$$Mn_2NO_2$ ($n$=1, 2, 3)/Au, the projection spectrum of FM is much larger, which also leads to a higher current in the FM state. The transmission of FM configuration is higher than that of AFM, so the GMR of Au/$n$$Mn_2NO_2$ ($n$=1, 2, 3)/Au is very high.

To more clearly reveal the deep-seated reasons for the formation of the GMR effect more clearly, we map the spin-resolved LDOS of the device in FM and the AFM states, taking Au/1$Mn_2NO_2$/Au as a typical example (Fig. 9). There is complete tunneling (minority-spin

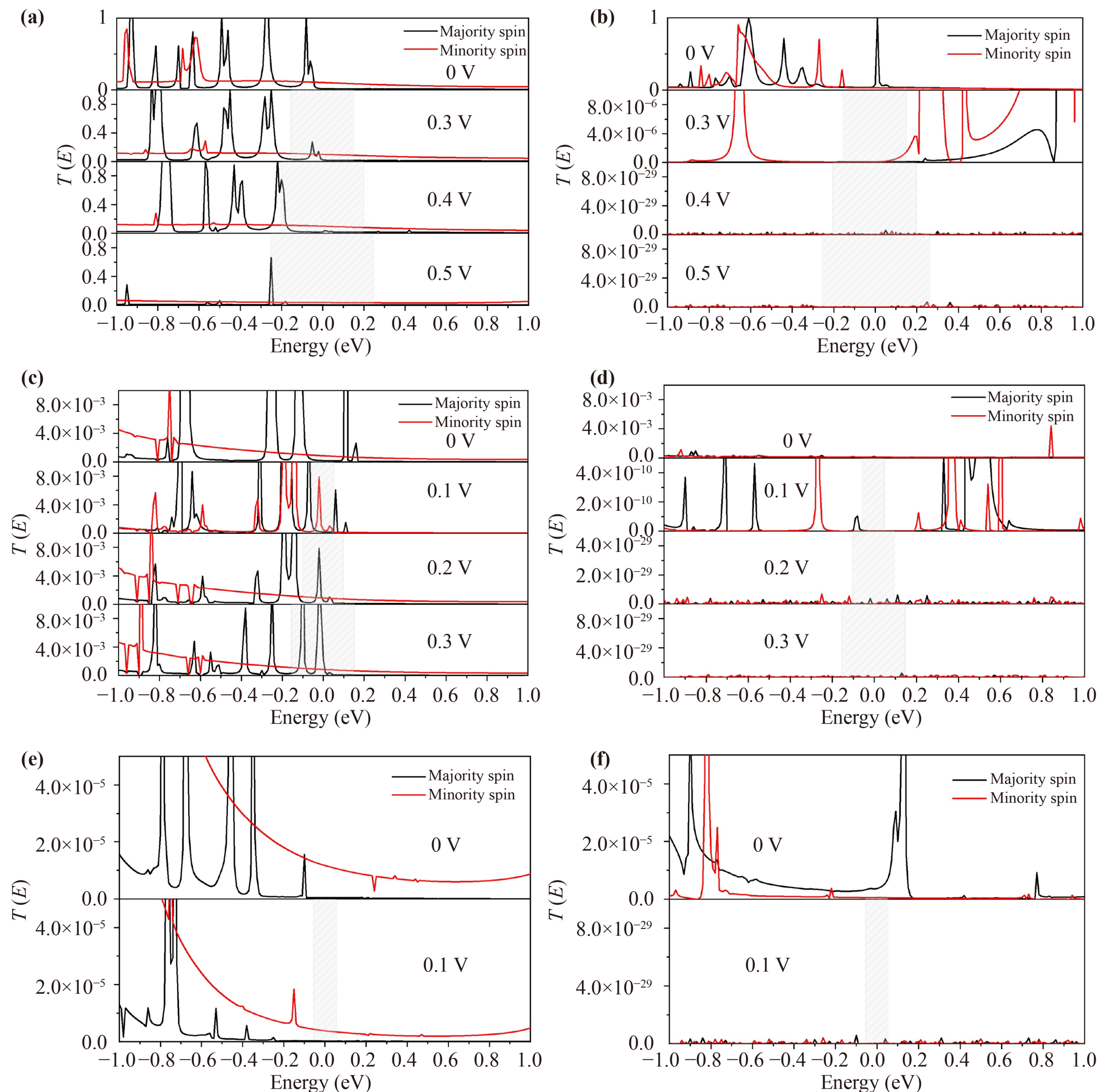


**Fig. 8** The relationship between the transmission spectrum of Au/$n$$Mn_2NO_2$ ($n$=1, 2, 3)/Au in the FM or AFM configuration and the bias voltage. **(a, b)** show monolayer device, **(c, d)** show bilayer device, and **(e, f)** show trilayer device.

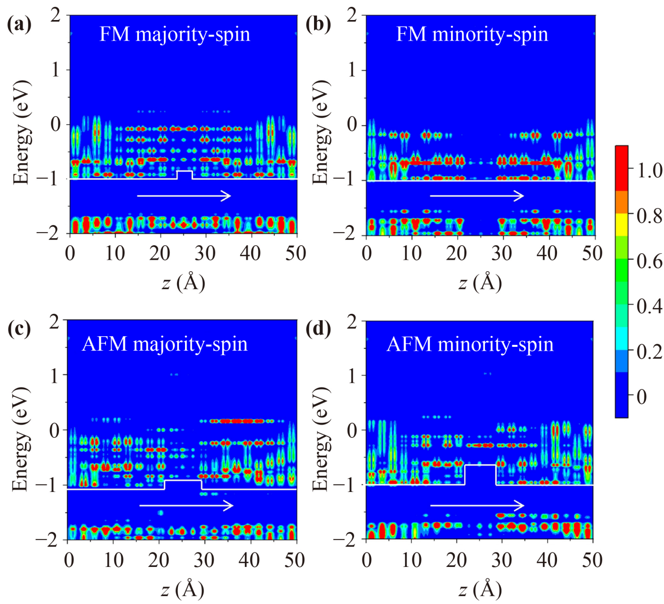


**Fig. 9** Spin-resolved projected LDOS of Au/1$Mn_2NO_2$/Au MTJ. FM state **(a)** majority-spin and **(b)** minority-spin projected LDOS, and **(c, d)** are AFM state majority-spin and minority-spin projected LDOS, respectively.

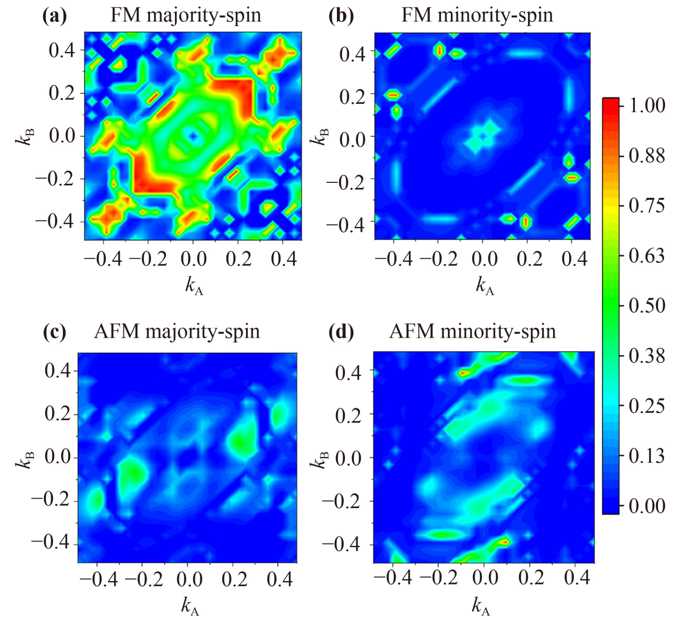


**Fig. 10** The spin-dependent transmission coefficient of Au/1$Mn_2NO_2$/Au MTJ in **(a, b)** FM and **(c, d)** AFM under zero bias.

channels) in the FM state, and the barrier height is almost 0 eV. In majority-spin channels, there is a small barrier of about 0.1 eV. In the AFM state, majority-spin channels have a smaller potential barrier of about 0.2 eV, while the minority-spin channels have a clear and larger potential barrier of 0.4 eV. Two spin electrons must pass through the barrier one by one: when the electron leaves the left electrode, majority-spin electrons in the FM state have a narrow barrier with a height of 0.1 eV, and minority-spin electrons have a barrier height of 0 eV. The barrier heights of the majority and minority spin electrons in the AFM state are 0.15 eV and 0.4 eV, respectively. These obstacles cause the total transmission probability in the AFM state to be less than the total transmission probability in the FM state. The number and size of potential barriers increase the difference between FM and AFM, and the transmission probability difference between the two states becomes larger, resulting in a huge value of GMR at low bias voltage.

To understand the GMR value near the zero bias voltage, we plot the Brillouin zone transmission coefficient $T$ ($k_A$, $k_B$) of the monolayer device at the 0 V Fermi level (Fig. 10). The color bar on the right represents the size of the transmission coefficient, and the maximum value of both the FM state and the AFM state reaches 1. For the FM state, the maximum value of majority-spin $T$ ($k_A$, $k_B$) is at (0.2, 0.2), (–0.2, –0.2), and the maximum value of minority-spin $T$ ($k_A$, $k_B$) is at (–0.4, 0.2), (–0.15, 0.4), (0.2, –0.4), (0.4, –0.2) on four points. For AFM, the maximum value of the minority-spin $T$ ($k_A$, $k_B$) is located at (–0.15, 0.4), and (0.15, –0.4), and the maximum area is smaller than the value area in FM. This produces a considerable transmission coefficient and conductance in FM, which in turn produces a large GMR.

To better learn the transmission state and transmission channel and its state at high GMR bias, we calculate the spatial distribution of the eigenvalues of Au/1$Mn_2NO_2$/Au molecular projection self-consistent Hamiltonian (MPSH). Since the monolayer device produces the highest GMR at 0.4 V, the eigenvalues we plot contributed to the current integration at 0.4 V. The isosurface value equals 0.03 to show the contribution of each atom in the highest occupied molecular orbital (HOMO) and the lowest unoccupied molecular orbital (LUMO). For the FM state under 0.4 bias, the range of the transport window is [–0.2 eV, 0.2 eV], and the effective eigenvalues are LUMO and LUMO+1 [Figs. 11(a) and (b)], HOMO-1 and HOMO-2 [Figs. 11(c) and (d)]. We can see that at 0.4 V bias, the four eigenstates of the FM state are not localized in the $x$ transport direction, showing excellent transport performance. However, for the AFM state, there is no electron energy level within the effective bias window, and there is no corresponding eigenstate, which is why the current is almost zero at 0.4 V.

## 4 Conclusion

In summary, the first-principles calculations and Keldish NEGF have been utilized to design an excellent GMR device using the half-metal $Mn_2NO_2$. The structure, electronic properties, current transmission, PLDOS, spin-dependent projection coefficient, and MPSH of the monolayer, bilayer, and trilayer devices have been subse-

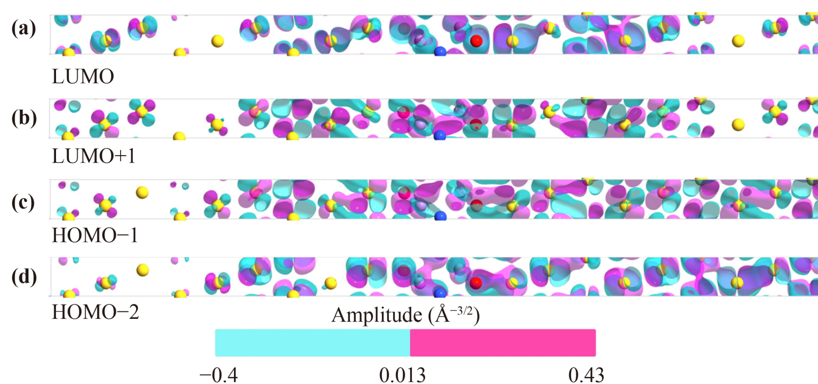


**Fig. 11** The spatial distribution of the MPSH eigenstates of the Au/1$Mn_2NO_2$/Au at 0.4 V. **(a, b)** MPSH of LUMO, LUMO+1. **(c, d)** MPSH of HOMO-1 and HOMO-2. The isosurface value sets to 0.03.

quently analyzed. The analysis of the electronic structure shows that the electrons in the FM state exhibit a high electron transmittance, while the electrons in AFM reveal a low transmittance. The attachment of the $Mn_2NO_2$ surface to Au (111) can alter the electronic structure of the Fermi level, however, it retains the half-metallic properties of $Mn_2NO_2$. The ultrahigh GMR value between the FM and AFM states of Au/$n$$Mn_2NO_2$ ($n$=1, 2, 3)/Au devices is noted to reach up to $1.15\times10^{31}\%$ and reaches the maximum at a small bias on increasing the number of layers, which imparts sensitivity the and energy-saving features to the device during practical applications. Moreover, in six configurations of the three devices, an obvious NDR effect is observed. In general, it has been demonstrated that $Mn_2NO_2$ is an ideal material for GMR applications, and the developed device is a spintronic device with the highest magnetoresistive ratio reported theoretically so far.

**Electronic supplementary materials** are available in the online version of this article at https://doi.org/10.1007/s11467-022-1184-z and https://journal.hep.com.cn/fop/EN/10.1007/s11467-022-1184-z and are accessible for authorized users.

**Acknowledgements** The authors would like to thank the National Natural Science Foundation of China (Grant Nos. 11704291 and 51875417), Hubei Province Key Laboratory of Systems Science in Metallurgical Process (Wuhan University of Science and Technology) (No. Y202101), and Key Laboratory of Nanodevices and Applications, Suzhou Institute of Nano-Tech and Nano-Bionics, Chinese Academy of Sciences (No. 21YZ03). The work was supported by High-Performance Computing Center of Wuhan University of Science and Technology. We thank ShiXiao Wen from HZWTECH for help and discussions regarding this study.

## References

1. Z. Wang, I. Gutiérrez-Lezama, N. Ubrig, M. Kroner, M. Gibertini, T. Taniguchi, K. Watanabe, A. Imamoğlu, E. Giannini, and A. F. Morpurgo, Very large tunneling magnetoresistance in layered magnetic semiconductor $CrI_3$, *Nat. Commun.* 9(1), 2516 (2018)
2. Y. Ni, K. L. Yao, C. Q. Tang, G. Y. Gao, H. H. Fu, and S. C. Zhu, Perfect spin-filter, spin-valve, switching and negative differential resistance in an organic molecular device with graphene leads, *RSC Adv.* 4(36), 18522 (2014)
3. L. N. Du, Z. C. Wang, and G. Z. Zhao, Novel intelligent devices: Two-dimensional materials based memristors, *Front. Phys.* 17(2), 23602 (2022)
4. Z. C. Zhou, F. Y. Yang, S. Wang, L. Wang, X. F. Wang, C. Wang, Y. Xie, and Q. Liu, Emerging of two-dimensional materials in novel memristor, *Front. Phys.* 17(2), 23204 (2022)
5. G. Y. Luo, X. Y. Lv, L. Wen, Z. Q. Li, and Z. B. Dai, Strain induced topological transitions in twisted double bilayer graphene, *Front. Phys.* 17(2), 23502 (2022)
6. L. Yin, X. C. Wang, and W. B. Mi, Ferromagnetic, ferroelectric and optical modulated multiple resistance states in multiferroic tunnel junctions, *ACS Appl. Mater. Interfaces* 11(1), 1057 (2019)
7. S. Yuasa, T. Nagahama, and Y. Suzuki, Spin-polarized resonant tunneling in magnetic tunnel junctions, *Science* 297(5579), 234 (2002)
8. M. F. Sun, X. C. Wang, and W. B. Mi, Large magnetoresistance in $Fe_3O_4$/4, 4'-bipyridine/$Fe_3O_4$ organic magnetic tunnel junctions, *J. Phys. Chem. C* 122(5), 3115 (2018)
9. D. Wijethunge, L. Zhang, C. Tang, and A. J. Du, Tuning band alignment and optical properties of 2D van der Waals heterostructure via ferroelectric polarization switching, *Front. Phys.* 15(6), 63504 (2020)
10. H. L. Yu, Z. G. Shao, Y. M. Tao, X. F. Jiang, Y. J. Dong, J. Zhang, Y. S. Liu, X. F. Yang, and D. J. Chen, Tunable tunneling magnetoresistance in in-plane double barrier magnetic tunnel junctions based on B vacancy h-NB nanoribbons, *Phys. Chem. Chem. Phys* 24, 3451 (2022)
11. J. W. Yan, S. Z. Wang, K. Xia, and Y. Q. Ke, Anomalous spin-dependent tunneling statistics in Fe/MgO/Fe junctions induced by disorder at the interface, *Phys. Rev. B* 97(1), 014404 (2018)
12. Y. Taniguchi, Y. Miura, K. Abe, and M. Shirai, Theoretical studies on spin-dependent conductance in FePt/MgO/

FePt(001) magnetic tunnel junctions, *IEEE Trans. Magn.* 44(11), 2585 (2008)
13. Z. Yan, R. Q. Zhang, X. L. Dong, S. F. Qi, and X. H. Xu, Significant tunneling magnetoresistance and excellent spin filtering effect in $CrI_3$-based van der Waals magnetic tunnel junctions, *Phys. Chem. Chem. Phys.* 22(26), 14773 (2020)
14. Y. L. Feng, X. M. Xu, and G. Y. Gao, High tunnel magnetoresistance based on 2D Dirac spin gapless semiconductor $VCl_3$, *Appl. Phys. Lett.* 116(2), 022402 (2020)
15. F. F. Li, B. S. Yang, Y. Zhu, X. F. Han, and Y. Yan, Ultrahigh tunneling magnetoresistance in van der Waals and lateral magnetic tunnel junctions formed by intrinsic ferromagnets $Li_{0.5}CrI_3$ and $CrI_3$, *Appl. Phys. Lett.* 117(2), 022412 (2020)
16. X. L. Zhang, P. W. Gong, F. Q. Liu, K. L. Yao, S. C. Zhu, and Y. Lu, Half-metallic of non-metal-adsorbed AsP and multifunctional two-dimensional spintronic device of impure AsP from first-principles calculations, *Physica E* 137, 115016 (2022)
17. C. D. Zheng, K. Jiang, K. L. Yao, S. C. Zhu, and K. M. Wu, The electromagnetic performance of transition metal-substituted monolayer black arsenic-phosphorus, *Phys. Chem. Chem. Phys.* 23(43), 24570 (2021)
18. S. C. Zhu, S. J. Peng, K. M. Wu, C. T. Yip, K. L. Yao, and C. H. Lam, Negative differential resistance, perfect spin-filtering effect and tunnel magnetoresistance in vanadium-doped zigzag blue phosphorus nanoribbons, *Phys. Chem. Chem. Phys.* 20(32), 21105 (2018)
19. E. Balcı, Ü. Ö. Akkus, and S. Berber, Controlling topological electronic structure of multifunctional MXene layer, *Appl. Phys. Lett.* 113(8), 083107 (2018)
20. E. Balcı, Ü. Ö. Akkus, and S. Berber, Band gap modification in doped MXene: $Sc_2CF_2$, *J. Mater. Chem. C* 5(24), 5956 (2017)
21. G. Wang and Y. Liao, Theoretical prediction of robust and intrinsic half-metallicity in $Ni_2N$ MXene with different types of surface terminations, *Appl. Surf. Sci.* 07, 249 (2017)
22. S. Chen, J. Zhou, and Z. M. Sun, Half-metallic ferromagnetism and surface functionalization-induced metal-insulator transition in graphene-like two-dimensional $Cr_2C$ crystals, *ACS Appl. Mater. Interfaces* 7(31), 17510 (2015)
23. G. Wang, Theoretical prediction of the intrinsic half-metallicity in surface-oxygen-passivated $Cr_2N$ MXene, *J. Phys. Chem. C* 120(33), 18850 (2016)
24. M. Naguib, O. Mashtalir, J. Carle, V. Presser, J. Lu, L. Hultman, Y. Gogotsi, and M. W. Barsoum, Two-dimensional transition metal carbides, *ACS Nano* 6(2), 1322 (2012)
25. M. Khazaei, A. Ranjbar, M. Arai, T. Sasaki, and S. Yunoki, Electronic properties and applications of MXenes: A theoretical review, *J. Mater. Chem. C* 5(10), 2488 (2017)
26. R. Qin, G. Shan, M. Hu, and W. Huang, Two-dimensional transition metal carbides and/or nitrides (MXenes) and their applications in sensors, *Mater. Today Phys.* 21, 100527 (2021)
27. R. Z. Qin, X. Li, M. J. Hu, G. C. Shan, R. Seeram, and M. Yin, Preparation of high-performance MXene/PVA-based flexible pressure sensors with adjustable sensitivity and sensing range, *Sens. Actuators A Phys.* 338, 113458 (2022)
28. Q. Q. Kong, X. G. An, L. Huang, X. L. Wang, W. Feng, S. Y. Qiu, Q. Y. Wang, and C. H. Sun, A DFT study of $Ti_3C_2O_2$ MXenes quantum dots supported on single layer graphene: Electronic structure and hydrogen evolution performance, *Front. Phys.* 16(5), 53506 (2021)
29. G. Wang and Y. Liao, Theoretical prediction of robust and intrinsic half-metallicity in $Ni_2N$ MXene with different types of surface terminations, *Appl. Surf. Sci.* 426, 804 (2017)
30. H. Kumar, N. C. Frey, L. Dong, B. Anasori, Y. Gogotsi, and V. B. Shenoy, Tunable magnetism and transport properties in nitride MXenes, *ACS Nano* 11(8), 7648 (2017)
31. G. Y. Gao, G. Q. Ding, J. Li, K. L. Yao, M. H. Wu, and M. C. Qian, Monolayer MXenes: Promising half-metals and spin gapless semiconductors, *Nanoscale* 8(16), 8986 (2016)
32. Y. W. Son, M. L. Cohen, and S. G. Louie, Half-metallic graphene nanoribbons, *Nature* 444(7117), 347 (2006)
33. X. X. Li, X. J. Wu, and J. L. Yang, Room-temperature half-metallicity in La (Mn,Zn)AsO alloy via element substitutions, *J. Am. Chem. Soc.* 136(15), 5664 (2014)
34. J. J. He, P. Lyu, and P. Nachtigall, New two-dimensional Mn-based MXenes with room-temperature ferromagnetism and half-metallicity, *J. Mater. Chem. C* 4(47), 11143 (2016)
35. J. H. Yang, S. Z. Zhang, A. P. Wang, R. N. Wang, C. K. Wang, G. P. Zhang, and L. Chen, High magnetoresistance in ultra-thin two-dimensional Cr-based MXenes, *Nanoscale* 10(41), 19492 (2018)
36. J. Yang, S. Fang, Y. Peng, S. Liu, B. Wu, R. Quhe, S. Ding, C. Yang, J. Ma, B. Shi, L. Xu, X. Sun, G. Tian, C. Wang, J. Shi, J. Lu, and J. Yang, Layer-dependent giant magnetoresistance in two-dimensional $CrPS_4$ magnetic tunnel junctions, *Phys. Rev. Appl.* 16(2), 024011 (2021)
37. L. F. Pan, L. Huang, M. Z. Zhong, X. W. Jiang, H. X. Deng, J. B. Li, J. B. Xia, and Z. M. Wei, Large tunneling magnetoresistance in magnetic tunneling junctions based on two-dimensional $CrX_3$ (X=Br, I) monolayers, *Nanoscale* 10(47), 22196 (2018)
38. J. Taylor, H. Guo, and J. Wang, *Ab initio* modeling of quantum transport properties of molecular electronic devices, *Phys. Rev. B* 63(24), 245407 (2001)
39. E. Balcı, Ü. Ö. Akkus, and S. Berber, High TMR in MXene-based $Mn_2CF_2/Ti_2CO_2/Mn_2CF_2$ magnetic tunneling junction, *ACS Appl. Mater. Interfaces* 11(3), 3609 (2019)